EES Solar

PAPER

View Article Online
View Journal

Cite this: DOI: 10.1039/d5el00064e

Straightforward and green synthesis of all-inorganic $CsPbI_3$ perovskite solar cells *via* nickel acetate incorporation

Jaume Noguera-Gómez, *[ab] Víctor Sagra-Rodríguez, [a] Marta Vallés-Pelarda, [ac] Miriam Minguez-Avellan, [a] Sandy Sánchez, [d] Rosario Vidal, [c] Jaume-Adrià Alberola-Borràs, [c] Rafael Abargues *[a] and Pablo P. Boix *[de]

Research on stable inorganic perovskite $CsPbI_3$ has emerged as a promising alternative to organic–inorganic hybrid perovskites due to its notable thermal stability and suitable bandgap (~1.73 eV) for single-junction and tandem solar cells in both indoor and outdoor applications. However, $CsPbI_3$ films with large grains and low trap densities are required to achieve high-performance and stable perovskite solar cells. In this study, we present a novel synthetic strategy in which nickel acetate ($Ni(AcO)_2 \cdot 4H_2O$) is incorporated in a pure DMSO $CsPbI_3$ precursor solution leading to the formation of stable γ-$CsPbI_3$ (black phase) nanocomposite perovskite films, as evidenced by XRD analysis. Moreover, the absence of detectable residual PbI_2 further confirms the enhanced conversion efficiency facilitated by $Ni(AcO)_2$ addition in our target when compared with pure $CsPbI_3$. Using this DMAI/HI-free approach, our top device with 0.1 M $Ni(AcO)_2$ (7.1 mol%) achieves over 12% power conversion efficiency in n–i–p mesoscopic configuration, with a lifespan exceeding 600 hours at maximum power point (MPP) and minimal losses (<20%) without encapsulation under controlled inert atmosphere. Besides, efficiencies over 15 and 17% are achieved under cool and warm white low-intensity illumination conditions, respectively, underscoring its potential for energy harvesting in indoor environments. The life cycle assessment (LCA) indicates that this new synthesis strategy reduces global warming potential (GWP) by 70% and eliminates hazardous chemicals like DMF and toluene. However, $Ni(AcO)_2$ and PbI_2 remain in the absorbing layer, requiring careful consideration.

Received 25th April 2025
Accepted 5th September 2025

DOI: 10.1039/d5el00064e

rsc.li/EESSolar

Broader context

Perovskite solar cells (PSCs) are rapidly advancing as a leading candidate for next-generation photovoltaic technologies. However, most state-of-the-art PSCs rely on organic–inorganic hybrid halide perovskites, which suffer from long-term stability issues, and rely on toxic solvents during fabrication. All-inorganic perovskites like $CsPbI_3$ offer superior thermal stability and are particularly promising for both outdoor and indoor energy harvesting applications, but their practical implementation has been hindered by phase instability and challenges in achieving high-quality films. This work addresses those challenges by introducing a new, environmentally friendly synthesis method using nickel acetate as a phase-directing additive in a DMF- and antisolvent-free formulation. The resulting γ-$CsPbI_3$ films exhibit improved crystallinity and enhanced stability, solar cells with efficiencies >12% without further passivation. Furthermore, the use of a greener fabrication route reduces the global warming potential by 70%, demonstrating that efficient and stable perovskite devices can be achieved without compromising environmental safety. These findings contribute to the ongoing transition toward sustainable and scalable PSC technologies, and highlight the potential of inorganic perovskites for clean energy generation beyond conventional settings.

Introduction

The interest in organic–inorganic halide perovskite solar cells (PSCs) has surged within the photovoltaics community, primarily driven by their impressive power conversion efficiencies (PCE) and the potential for low-cost facile fabrication processes. Since their debut in 2009, when initial efficiencies were a modest 3–4%,[1] advancements in this technology have rapidly increased PCE values, with the highest certified efficiency now reaching 26.1%.[2] These materials typically feature a structure consisting of organic and inorganic cations like

[a]Instituto de Ciencia de los Materiales, Universidad de Valencia, Catedrático José Beltrán, 2, València, 46071, Spain. E-mail: rafael.abargues@uv.es
[b]Energy Research Institute @ NTU, Nanyang Technological University, Research Techno Plaza, 637553, Singapore. E-mail: jaume.ng@ntu.edu.sg
[c]Institute of Advanced Materials (INAM), University Jaume I, Av. De Vicent Sos Baynat s/n, 12006 Castelló de la Plana, Spain
[d]Laboratory for Molecular Engineering of Optoelectronic Nanomaterials, Institute of Chemistry and Chemical Engineering, École Polytechnique Fédérale de Lausanne, 1015 Lausanne, Switzerland. E-mail: Pablo.P.Boix@itq.upv.es
[e]Instituto de Tecnología Química, Universitat Politècnica València-Consejo Superior de Investigaciones Científicas, Av. dels Tarongers, 46022 València, Spain

methylammonium (MA^+), formamidinium (FA^+), and cesium (Cs^+) within a lead halide framework. However, despite their high efficiency, these hybrid perovskite structures are plagued by stability issues that undermine their long-term viability. In terms of commercialization, solar modules must endure wide operational stress factors such as temperature, light exposure (visible and UV), and electrical bias (outlined in the standard ISOS stability protocols), as these are critical concerns for their stability.[3–7]

In recent years, fully inorganic cesium lead halide perovskites, and particularly $CsPbI_3$, have emerged as a potential candidate due to their exceptional thermal stability.[8–12] $CsPbI_3$ is especially promising due to its bandgap of 1.73 eV, making it suitable for applications in double-junction perovskite/silicon tandem solar cells in both indoor and outdoor photovoltaic applications.[3,13–15] The maximum theoretical efficiency under varying light conditions can be determined by adapting the Shockley–Queisser limit to different irradiation spectra.[16] Notably, this efficiency limit increases from 33% under sunlight illumination to 57% under indoor lighting conditions.[17]

The current best research PCEs for these all-inorganic perovskite absorbers are around 21%.[18,19] However, $CsPbI_3$ faces significant challenges in maintaining a stable perovskite phase at ambient temperatures due to the small ionic radius of cesium, which results in structural instability. This structural instability poses a significant drawback for long-term photovoltaic applications.[20] Furthermore, certain synthetic routes require annealing temperatures exceeding 350 °C to achieve the α-$CsPbI_3$ phase, rendering it impractical for use with various device architectures, including different substrates and charge transport layers.[15,21,22] In this sense, low-temperature processing benefits tandem solar cell fabrication, reducing energy consumption, simplifying operation, improving reproducibility, and enabling sustainable industrial scalability.[14]

Innovations in material processing and stabilization methods have paved the way for obtaining $CsPbI_3$ perovskite black phases at lower temperatures to become a viable alternative to their hybrid counterparts, offering a path toward more thermally stable and efficient photovoltaic technologies. The different reported strategies to stabilize $CsPbI_3$ black phases include solvent engineering,[23,24] surface passivation engineering modifying the surface tension,[25] dimensionality engineering (scaffold confinement,[26] nanocrystal colloidal approaches[11] and quasi-2D by incorporating large organic cations[27,28]) or chemical engineering (small molecules[29–33] and ionic incorporation partially replacing lead with other divalent cations ($CsPb_xM_{1-x}I_3$)[34,35] or substituting some iodide with bromide[36]). Among them, the most widespread one for the fabrication of high-efficiency PSCs at relatively low temperature relies on the addition of dimethylammonium iodide (DMAI) as (DMA_xCs_{1-x})PbI_3. DMAI has demonstrated the ability to stabilize and influence the crystallinity and grain size of the $CsPbI_3$ perovskite black phases.[33] This was first reported by Eperon *et al.* 2015 who introduced hydroiodic acid (HI) as an additive[37] that, in subsequent studies, was identified to generate *in situ* DMAI as a decomposition product of DMF through acidic hydrolysis catalyzed by HI.[38] Although high annealing temperatures are sometimes necessary to fully volatilize the organic additives and promote phase transitions in $CsPbI_3$,[39] many high-efficiency devices exceeding 20% power conversion efficiency are fabricated by incorporating DMAI, which aid in phase stabilization during processing.[20,40,41] In this scenario, there is still ongoing debate about whether DMAI-assisted $CsPbI_3$ perovskites are fully inorganic materials or instead represent $Cs_{1-x}DMA_xPbI_3$ mixed-cation or "cesium-rich" systems.[42,43]

Recently, we have demonstrated the potential of a nickel acetate-based matrix for the *in situ* synthesis and stabilization of perovskite nanocrystals through a simple and efficient process.[44–48] In this approach, nanocrystal size was primarily controlled by adjusting the relative concentrations of perovskite precursors and $Ni(AcO)_2$, as well as factors such as relative humidity during synthesis. Expanding on these findings, we investigated $Ni(AcO)_2$ for the synthesis of large-grain perovskites for photovoltaics, particularly for materials with metastable polymorphic phases like the γ-$CsPbI_3$ black phase. We present a promising DMSO-only, DMAI/HI-free precursor solution strategy incorporating $Ni(AcO)_2$ to drive the crystallization and stabilization of γ-$CsPbI_3$ in a nanocomposite. Our results show that increasing grain size to a level suitable for photovoltaic applications requires an excess of perovskite precursors with respect to $Ni(AcO)_2$. We demonstrate a significant correlation between the concentration of $Ni(AcO)_2$ and the stabilization of the γ-$CsPbI_3$ black phase in comparison with pristine $CsPbI_3$. As confirmed through X-ray diffraction (XRD) analysis, the role of $Ni(AcO)_2$ directly impacts the crystallization process. EDX analysis also confirms a homogeneous distribution of $Ni(AcO)_2$ around the perovskite grains. Through SEM, we observe the effect of the annealing temperature and concentration impacting the grain size in the perovskite absorber layer. JV curves further confirm a $Ni(AcO)_2$ concentration threshold for optimal device performance without compromising the charge extraction. Finally, using this method, our best device, containing 0.1 M $Ni(AcO)_2$ (7.1 mol%), achieves a power conversion efficiency (PCE) of over 12% in n–i–p configuration without any passivation or surface modification, maintaining a lifespan of more than 600 hours at maximum power point (MPP) with minimal losses below 20%. Besides, its adequacy to work under enhanced low-intensity lighting conditions has been tested, achieving PCEs over 15 and 17% under cool and warm white illuminations, respectively. The life cycle assessment (LCA) indicates that the approach reduces global warming potential (GWP) by 70% and minimizes impacts across most categories, despite the inclusion of $Ni(AcO)_2 \cdot 4H_2O$, which has low toxicity compared to PbI_2. Furthermore, the DMSO-only, DMAI/HI-free approach avoids hazardous substances like DMF, toluene, and TOPO (used in a comparative synthesis approach). However, caution is warranted as $Ni(AcO)_2 \cdot 4H_2O$ and PbI_2 remain in the absorbing layer.

Results and discussion

In situ synthesis of $CsPbI_3$-nanocomposite films

γ-$CsPbI_3$ nanocomposite films are synthesized by a solution-based approach from a precursor solution of CsI, PbI_2, and

$Ni(AcO)_2$ in DMSO. The precursor solution is spin-coated onto a substrate, followed by rapid thermal annealing to crystallize the γ-$CsPbI_3$ phase. Fig. 1 provides an overview of the general *in situ* synthesis process for the nanocomposite, illustrating the synthetic approach for $CsPbI_3$ and highlighting the effect of $Ni(AcO)_2$ on the perovskite nanocomposite crystallization.

Achieving an optimal grain size for photovoltaic applications necessitates an excess of perovskite precursors relative to $Ni(AcO)_2$. Excess $Ni(AcO)_2$ can limit the growth of large grains by disrupting the perovskite framework. A controlled precursor ratio is, therefore, critical to balancing grain growth while maintaining structural stability. Therefore, we have tested different $Ni(AcO)_2$ concentrations ranging from 3.7 to 38.1 mol% within $CsPbI_3$, ensuring an excess of perovskite in the final film. This approach allowed us to systematically evaluate the impact of $Ni(AcO)_2$ on the crystallization process, lattice structure, grain growth, and stability of $CsPbI_3$.

Optical properties of the nanocomposite perovskite films

The effect of $Ni(AcO)_2$ concentration and annealing times on the optical properties of the perovskite films are studied at an annealing temperature of 200 °C. For all evaluated conditions, the $CsPbI_3$ concentration is kept constant at 1.3 M to ensure a consistent assessment of the effects of $Ni(AcO)_2$ concentration on the final layer properties. We first examined the annealing time at 200 °C, a temperature slightly above the boiling point of DMSO (189 °C), to ensure its effective removal and a complete phase transition to γ-$CsPbI_3$ phase.[9]

Fig. 2a shows films prepared with different $Ni(AcO)_2$ concentrations and various annealing times at 200 °C. For all concentrations, the formation of the γ-phase is observed after just 5 s, indicating a rapid crystallization to the γ-$CsPbI_3$ phase. However, as the annealing time increases, films with a $Ni(AcO)_2$ concentration of 0.05 M (3.7 mol%) change from black to yellow, suggesting the transformation to the non-perovskite yellow phase. In contrast, from concentrations 0.1 M (7.1 mol%) and higher, the γ-phase remains stable for longer bake times, indicating $Ni(AcO)_2$ improves not only γ-$CsPbI_3$ crystallization but also the γ-phase stability.

UV-vis spectroscopy confirms the fast crystallization of the black γ-$CsPbI_3$ phase for samples baked at 200 °C in the presence of $Ni(AcO)_2$. After just 5 seconds, we observe the characteristic absorption band at 680 nm corresponding to γ-$CsPbI_3$ in all samples with $Ni(AcO)_2$ (Fig. 2b). The control sample without $Ni(AcO)_2$ does not crystallize into the γ-$CsPbI_3$ (Fig. 2c). The excitonic band intensity increases with the annealing time. For a 0.1 M $Ni(AcO)_2$ (7.1 mol%), we observe the absorption excitonic band reaching its maximum at 10 s. However, for longer baking times, 20 s, phase degradation occurs, leading to the formation of the non-perovskite yellow phase (δ-$CsPbI_3$), and a decrease in the absorption band (Fig. 2b). A comparison of their optical properties between pristine $CsPbI_3$ and γ-$CsPbI_3$-$Ni(AcO)_2$ nanocomposite is shown in Fig. 2c. As expected, the pristine δ-$CsPbI_3$ does not display photoluminescence (PL), whereas the γ-$CsPbI_3$-$Ni(AcO)_2$ nanocomposite exhibits a PL peak centered at approximately 720 nm. The same trend is observed for different concentrations of $Ni(AcO)_2$. However, at 0.05 M $Ni(AcO)_2$ (3.7 mol%), a partial transformation of γ-$CsPbI_3$ is initially observed, but the yellow δ-phase forms after a few seconds (see Fig. 2a), which is further confirmed by XRD in the structural characterization section. This confirms that $Ni(AcO)_2$ plays a determining role in the crystallization and stability of γ-$CsPbI_3$. The optimal composition is 1.3 M $CsPbI_3$: 0.1 M $Ni(AcO)_2$ (92.9 mol% $CsPbI_3$ and 7.1 mol% $Ni(AcO)_2$), annealed at 200 °C for 10 s. This concentration has been identified as a critical threshold for maintaining both crystallinity and stability, as further confirmed in the photovoltaic performance (see device characterization section, *J–V* curves, Fig. 4b). Beyond this threshold, the current density significantly declines faster, attributed to reduced charge carrier mobility associated with the excessive $Ni(AcO)_2$ content. This leads to poor grain interconnectivity, which significantly hinders its suitability for application as PSCs, as detailed in the subsequent sections.

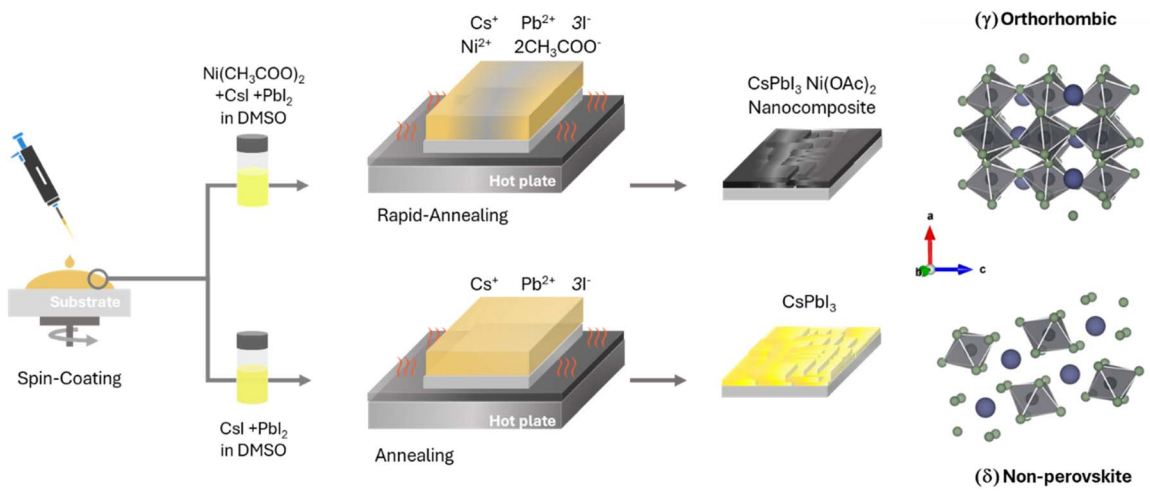

Fig. 1 Synthetic approach for $CsPbI_3$ nanocomposites, emphasizing the impact of $Ni(AcO)_2$ doping on perovskite crystallization.

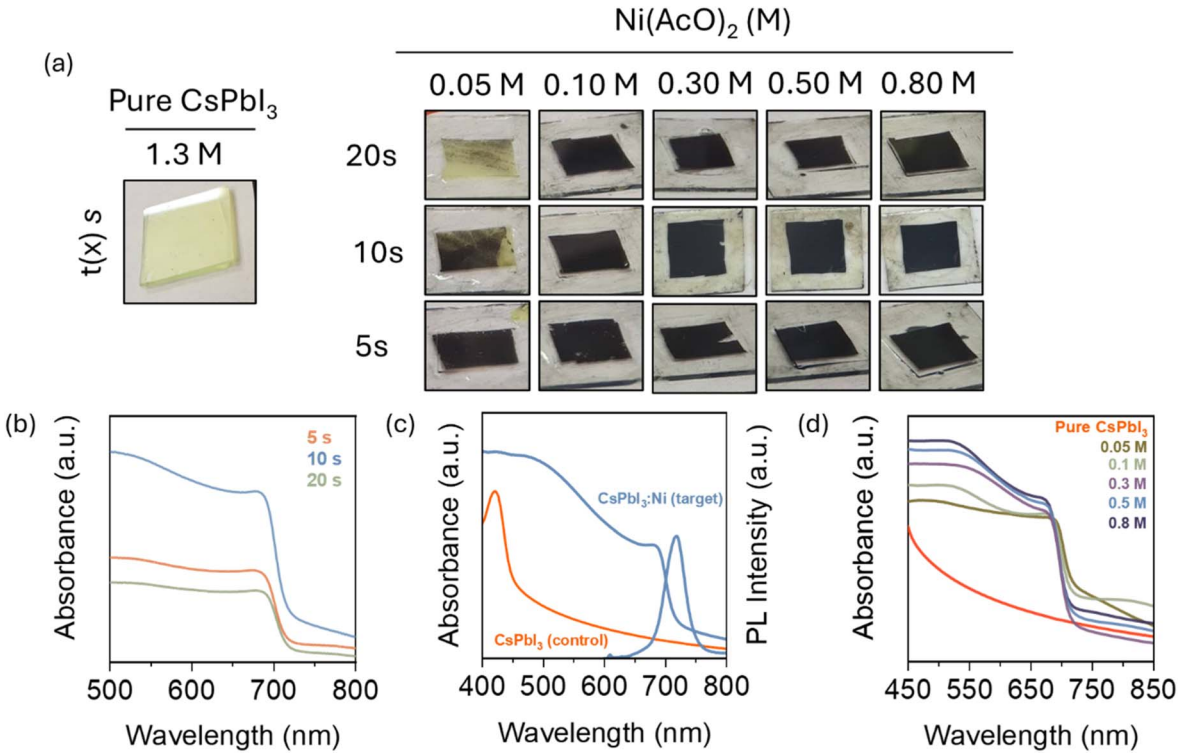

Fig. 2 Impact of annealing time and concentration on $CsPbI_3$ films. (a) Photographic images of pristine $CsPbI_3$ and $CsPbI_3$–$Ni(AcO)_2$ films annealed at 200 °C for different times and $Ni(AcO)_2$ concentrations. (b) Annealing time dependency in UV-vis absorption spectra for 0.1 M (7.1 mol%) $Ni(AcO)_2$ concentration. (c) UV-vis absorption spectra and PL spectra comparison for the control and the target nanocomposite annealed at 200 °C for 10 s. (d) Nanocomposite UV-vis absorption spectra *vs.* $Ni(AcO)_2$ concentration annealed at 200 °C for 10 s.

We have calculated the optical bandgap (E_g) of γ-$CsPbI_3$-$Ni(AcO)_2$ nanocomposite thin films from Fig. 2d by simulating the absorption spectra near the band edge using Elliott's formula (see SI).[49] The absorption spectra (Fig. S1) shows that increasing the $Ni(AcO)_2$ concentration shifts the optical E_g to higher energies (Table S1). This shift is attributed to significant random microstrain[50] within the perovskite grains, as evidenced by the broadening of XRD peaks, which will be discussed in the following section. This strain plays a crucial role in stabilizing the γ-$CsPbI_3$ phase, a topic explored further in the next section.

Structural and morphological characterization

The concentration of $Ni(AcO)_2$ plays a crucial role in modulating the optical properties of γ-$CsPbI_3$. To investigate this effect, we have conducted XRD analyses of $CsPbI_3$ nanocomposites synthesized with varying $Ni(AcO)_2$ concentrations at different annealing temperatures to determine the optimal conditions for γ-$CsPbI_3$ formation. The XRD diffractograms (Fig. 3) reveal how annealing temperature influences the crystallinity of the γ-$CsPbI_3$ phase, effectively suppressing transitions to the non-perovskite δ-phase (Fig. 3a). These structural insights align well with the observed optical properties.

For all temperatures, we found characteristic peaks corresponding to the orthorhombic γ-phase near 14.3°, 20.8°, and 28.9°, which can be assigned to the (020), (002), and (202) planes, respectively (ICSD no. 434 338). At 250 °C, a phase transition is observed, evidenced by the appearance of a weak diffraction peak at 13.1°, which corresponds to the (102) plane of the δ-$CsPbI_3$ phase (Fig. 3b) (ICSD no. 250744).

Regarding the crystallization mechanism, we observe the formation of an intermediate 0D Cs_4PbI_6 phase at lower temperatures. As shown in Fig. 3c, the characteristic peaks of the 0D Cs_4PbI_6 phase at 11.9° and 28.6° at 100 and 150 °C, disappear at higher temperatures. This observation suggests that Cs_4PbI_6 acts as a template in the phase conversion of $CsPbI_3$. This is consistent with a study of an intermediate formamidine acetate by Duan *et al.* 2022.[32] At 200 °C, the 0D intermediate phase is fully removed, leaving only the γ-$CsPbI_3$ phase. These observations align with our previous findings, which highlighted the role of the $Ni(AcO)_2$ in the transformation of a 0D intermediate phase to the corresponding 3D perovskite phase by the presence of acetate groups.[47]

We observe that higher temperatures improve crystallinity and peak intensity. As observed in SEM, annealing at 200 °C promotes the formation of larger γ-$CsPbI_3$ grains, which is favorable for enhancing carrier mobility and overall device performance.[51] Therefore 200 °C is the optimal temperature target for synthesizing γ-$CsPbI_3$.

The formation of the γ-$CsPbI_3$ phase is also strongly influenced by the amount of $Ni(AcO)_2$. The effect of $Ni(AcO)_2$ concentration is also examined in samples annealed at 200 °C for 10 s. XRD diffractograms of films with $Ni(AcO)_2$ concentrations below 0.1 M (7.1 mol%) reveal residual peaks of the δ-

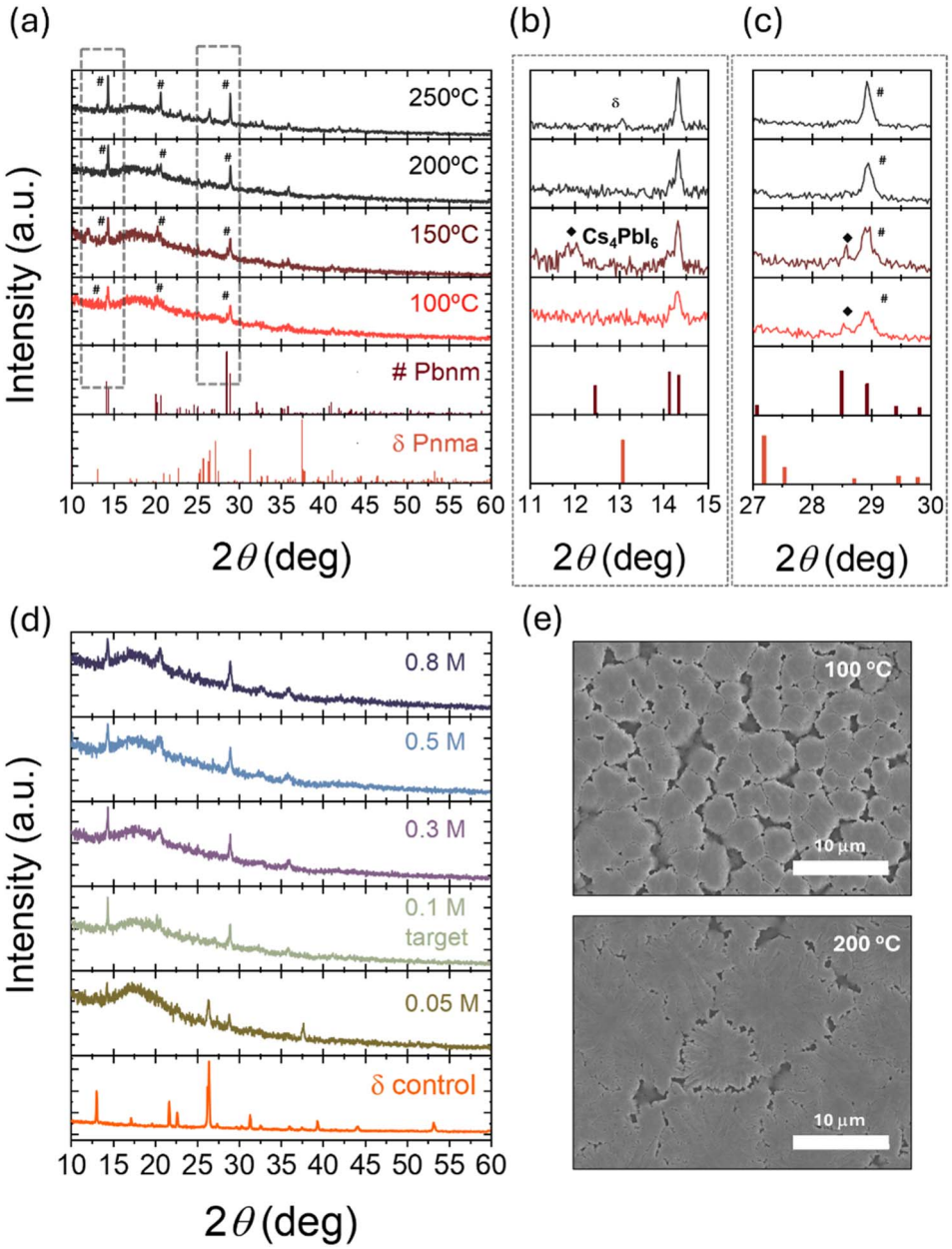

Fig. 3 XRD patterns of $CsPbI_3$–$Ni(AcO)_2$ nanocomposites. (a–c) Annealing temperature impact on 0.1 M $Ni(AcO)_2$ for 10 s. (d) Effect of $Ni(AcO)_2$ concentration annealed at 200 °C for 10 s. (e) SEM images of 0.1 M $Ni(AcO)_2$ nanocomposite at 100 and 200 °C for 10 s.

phase, indicating an incomplete phase transition or poor stabilization of the γ-$CsPbI_3$ phase (Fig. 3d). When the concentration exceeds 0.1 M (7.1 mol%), the orthorhombic peaks become more intense and sharper, indicating improved crystallinity (Fig. 3d).

The role of Ni^{2+} in the crystallographic structure can also be assessed in this context. Partial exchange of Pb^{2+} (~120 pm) with smaller Ni^{2+} (~72 pm) would typically induce lattice contraction, resulting in a shift of XRD peaks to higher 2θ values. However, the absence of a significant shift eliminates the possibility of partial substitution within the $CsPbI_3$ lattice and makes it highly unlikely.[52]

A detailed analysis of peak broadening for different $Ni(AcO)_2$ concentrations has been conducted. The crystallite size (D) and microstrain (ε) are determined using Williamson–Hall plots (Fig. S2). Increasing the $Ni(AcO)_2$ concentration from 0.05 to 0.8 M (3.7 to 38.1 mol%) leads to a reduction in grain domain size from 61 to 30 nm, together with a corresponding increase in microstrain.[50] The microstrain induced by $Ni(AcO)_2$ incorporation kinetically hinders the transformation from the γ to the δ-phase, enhancing phase stability as $Ni(AcO)_2$ concentration increases. This trend is consistent with Elliott's bandgap calculations (Table S1), which indicate a shift toward higher energies with increasing $Ni(AcO)_2$ concentration, and with the SEM images, which show a decrease in particle size as the $Ni(AcO)_2$ content increases (Fig. S4). This suggests that the presence of acetate could facilitate the formation of additional

nucleation sites of the γ-$CsPbI_3$ and, consequently, lead to a narrower grain size distribution in the perovskite films.

Additionally, to assess the structural stability of $CsPbI_3$ perovskite films incorporating $Ni(AcO)_2$ under ambient conditions, we have conducted time-resolved XRD of target $CsPbI_3$ film exposed to 60% RH at 25 °C measuring samples immediately after glovebox removal and every 10 minutes thereafter (Fig. S3). Fresh films exhibit a single peak at 14.3°, corresponding exclusively to the γ-$CsPbI_3$ phase, with no secondary phases detected. Over time, new peaks at ~9.8° and ~12.9° appear, corresponding to the δ-$CsPbI_3$ phase and PbI_2, respectively. This indicates moisture-driven degradation of the perovskite structure toward more thermodynamically stable phases, while preserving the γ-$CsPbI_3$ phase under inert conditions, emphasizing the impact of humidity on film stability.

Scanning Electron Microscopy (SEM) images (Fig. 3e) revealed significant differences in the microstructure and morphology of the nanocomposite for 100 °C and 200 °C annealing temperature. We observe the formation of larger grains and more compact films at 200 °C. We attribute the reduced grain size at lower temperatures to incomplete crystallization of perovskite due to inefficient DMSO removal. Larger grains and more compact films are advantageous for device performance by reducing grain boundary defects and consequently minimizing recombination centers and enhancing charge carriers mobility.[51]

Energy-dispersive X-ray (EDX) analysis (Fig. S5) further corroborates the uniform distribution of $Ni(AcO)_2$ across the perovskite grains. Elemental mapping reveals a consistent presence of Ni homogeneously distributed throughout the entire grain structure, with no noticeable aggregation or phase separation. This homogeneity suggests that Ni^{2+} is primarily localized around the perovskite grains rather than substituting within the crystal lattice. This conclusion aligns with the XRD results, where the crystallographic peaks remain unchanged, indicating that Ni^{2+} does not significantly alter the perovskite structure but instead surrounds the grains. This distribution may play a key role in enhancing the material's stability and influencing its electronic properties.

XPS analysis has been conducted to investigate the variation in lattice binding energy of $CsPbI_3$ with and without $Ni(AcO)_2$ (Fig. S6). The Cs 3d, Pb 4f, and I 3d peaks consistently shift to lower binding energies upon the addition of $Ni(AcO)_2$. This shift can be attributed to an increase in electron density on the surface of $CsPbI_3$, due likely to electron transfer from Ni atoms to the perovskite lattice. The increased surface charge density induced by $Ni(AcO)_2$ addition reduces the surface tension of $CsPbI_3$, consequently lowering the surface free energy.[29] This modification plays a crucial role in stabilizing the γ-$CsPbI_3$ phase in our synthesis approach.

To gain broader insight into the role of acetate salts in stabilizing γ-$CsPbI_3$ beyond $Ni(AcO)_2$, preliminary fundamental studies have been conducted exploring the use of alternative metal acetates under identical DMSO only synthesis route. Specifically, $Co(AcO)_2 \cdot 4H_2O$ and $Zn(AcO)_2 \cdot 2H_2O$ have been evaluated alongside $Ni(AcO)_2$ to assess how the nature of the metal and acetate group influence the optical, structural, and morphological properties of the resulting perovskite films (Fig. S7). The $Co(AcO)_2$-based γ-$CsPbI_3$ film exhibits a very similar absorption profile, closely matching that of $Ni(AcO)_2$ in both onset and shape, suggesting comparable optical quality and phase formation (see Fig. S7a). In contrast, the film with $Zn(AcO)_2$ shows a less pronounced excitonic feature and a blue-shifted absorption onset, indicating poorer crystallinity or the presence of a different phase. XRD patterns (Fig. S7b) revealed that both Co and Zn acetates promoted partial γ-phase formation, though residual δ-phase and PbI_2 reflections persisted. SEM images (Fig. S7c) show moderately cohesive grains for $Co(AcO)_2$ and poorly cohesive grains for $Zn(AcO)_2$. We hypothesize that stabilization arises from a combination of factors, including waters of crystallization, acetate ligand basicity, and salt hygroscopicity.[47] While these findings provide valuable insights into the role of metal acetates in phase stabilization, further detailed investigations will be essential to fully elucidate the underlying mechanisms and optimize material performance.

Photovoltaic characterization

We tested the performance of $CsPbI_3$–$Ni(AcO)_2$ devices in n–i–p configuration for different $Ni(AcO)_2$ concentrations. The device structure consisted of FTO/c-TiO_2/m-TiO_2/perovskite/Spiro-OMeTAD/Au (Fig. 4a). A cross-section image of the complete device stack is provided in the SI (Fig. S8). Fig. 4b shows the statistical data of different devices prepared from 0.05 to 0.8 M $Ni(AcO)_2$ (3.7 to 38.1 mol%). Across a range of concentrations, the curves show a volcano-shaped dependence on concentration. The best photovoltaic performance is achieved for 0.1 M $Ni(AcO)_2$. The champion SC has J_{sc}, V_{oc}, and FF values of 17.6 mA cm^{-2}, 1.03 V, and 68.13%, respectively, corresponding to a PCE of 12.43%. The *J–V* curve and statistics are shown in Fig. 4c. These findings are in good agreement with XRD results: at 0.05 M $Ni(AcO)_2$, both δ-$CsPbI_3$ and γ-$CsPbI_3$ phase perovskite phases coexist. The non-perovskite δ-$CsPbI_3$ phase avoids an effective charge transport within the absorber, leading to non-optimal electrical performance. Similarly, above 0.1 M $Ni(AcO)_2$ (7.1 mol%), we observe a rapid drop in the current density. While a higher $Ni(AcO)_2$ concentration enhances the stability of the orthorhombic γ-$CsPbI_3$ phase (see Fig. S9), photovoltaic performance is compromised. We attribute the decrease in PV performance to the active role of $Ni(AcO)_2$ in stabilizing the γ-$CsPbI_3$ phase while simultaneously promoting the separation of perovskite grains. Because $Ni(AcO)_2$ is an insulating material, the resulting composite shows a poorer electrical interconnection among grains, which hinders charge extraction. EDX analysis (Fig. S5) further supports this interpretation by confirming the uniform distribution of $Ni(AcO)_2$ around the perovskite grains. This phenomenon has been previously observed in studies involving $Ni(AcO)_2$ matrices.[46]

In addition, we have conducted a light stability test on an unencapsulated device under ambient conditions in an inert nitrogen atmosphere, with constant 1-sun illumination. The target $CsPbI_3$–$Ni(AcO)_2$ device maintained approximately 80% of its initial efficiency after 600 hours of continuous light exposure measured at a fixed voltage near the MPP (Fig. 4d).

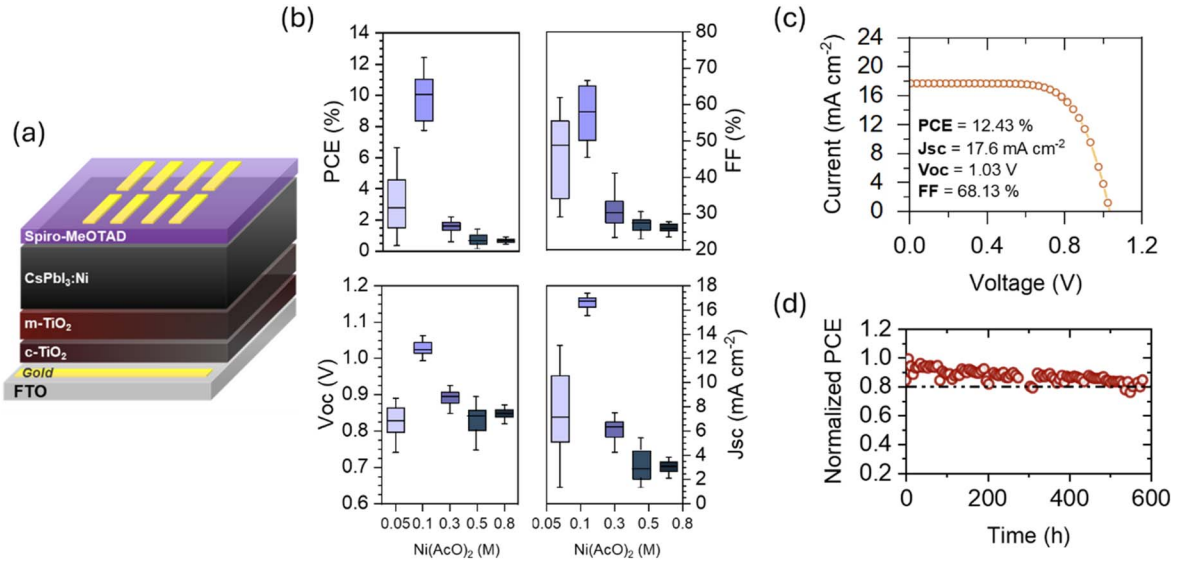

Fig. 4 (a) Device structure: FTO/c-TiO_2/m-TiO_2/$CsPbI_3$: $Ni(AcO)_2$/Spiro-OMeTAD/Au. (b) Statistical data of devices with different $CsPbI_3$: $Ni(AcO)_2$ ratios. (c) *J*–*V* curve of the champion device. (d) Light stability test on unencapsulated devices under N_2 conditions, with constant 1-sun illumination at 30 °C.

Additional analysis is conducted to investigate the ideality factor (n_{id}) of the solar cells studied at different $Ni(AcO)_2$ concentrations, providing deeper insights into the dominant recombination mechanisms influencing device performance. The ideality factor is determined from the dependence of the open-circuit voltage V_{OC} on light intensity, as described in Fig. S10.[53] At low concentrations of $Ni(AcO)_2$ (0.05 M), the ideality factor reaches 2.2, indicating dominant trap-assisted recombination and poor material quality, primarily attributed to the coexistence of both delta and gamma phases. For higher $Ni(AcO)_2$ concentrations (0.1 M) the ideality factor decreases to 1.7, suggesting Shockley–Read–Hall (SRH) recombination within the bulk as the dominant loss mechanism, which aligns with previously reported observations on $CsPbI_3$ solar cells.[53–55] When increasing $Ni(AcO)_2$ concentrations to 0.3 M, the ideality factor further decreases to ~1.5. However, this reduction coincides with deteriorated device performance, suggesting the emergence of interfacial recombination issues that correlate with charge transport limitations at higher $Ni(AcO)_2$ concentrations, as discussed previously.

Low-intensity illumination studies

To explore the potential of this synthesis approach, performance measurements have been conducted on the optimum γ-$CsPbI_3$-$Ni(AcO)_2$ nanocomposite solar cell under both cool white and warm white low-intensity illumination. These enhanced indoor light sources with different irradiance spectra (Fig. S11a) achieve peak efficiencies with semiconductor materials featuring bandgaps between 1.7 and 1.8 eV (Fig. S11b), in contrast to the optimal 1.4 eV bandgap for solar illumination. In this context, our best $CsPbI_3$–$Ni(AcO)_2$ devices achieve remarkable efficiencies of 15.4% under commercial based cool white (23 mW cm^{-2}) and 17.6% under warm white (13 mW cm^{-2}) lighting. PSC parameters and *J*–*V* curves for low-intensity illumination measurements are gathered in Table 1 and Fig. 5, respectively. These results further confirm the potential of all-inorganic $CsPbI_3$-based perovskites for indoor applications, demonstrating strong alignment with theoretical efficiency predictions.

Table 1 PSC parameters upon exposure to different light conditions of γ-$CsPbI_3$-$Ni(AcO)_2$ nanocomposite solar cell (7.1 mol% $Ni(AcO)_2$)

Illumination conditions	PCE (%)	FF (%)	J_{sc} (mA cm^{-2})	V_{oc} (V)
1 Sun (100 mW cm^{-2})	10.0	70	14.2	1.02
Cool white (23 mW cm^{-2})	15.4	71	5.3	0.96
Warm white (13 mW cm^{-2})	17.6	76	3.2	0.94

Life cycle assessment

The environmental impacts associated with the synthesis and deposition process of $CsPbI_3$ with $Ni(AcO)_2$ are evaluated using the LCA methodology, conducted in accordance with EN-ISO standards (14 040/14 044) and the IEA PVPS guidelines.[56] This evaluation is juxtaposed with that of the synthesis and deposition of $CsPbI_3$ with DMAI.[57]

The functional unit for both cases is 1 cm^2. The absorber layer is the only one considered in the indoor solar cell. The electron and hole transport layer, electrodes, and substrate are the same for the two methods, so they are not included in the comparative assessment. The SI note presents life cycle inventories and evaluation impacts with the method Environmental Footprint, EF 3.0.[58]

The addition of $Ni(AcO)_2$ to the $CsPbI_3$ solution avoids the use of several harmful substances compared to the DMAI method: DMAI, MACl, OAI and TOPO.[57] The number of spin coating processes employed is reduced from 4 to 1, the heating

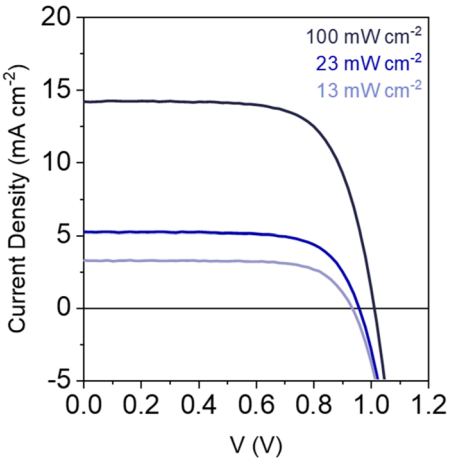

Fig. 5 *J–V* curves under different light conditions of target $CsPbI_3$–$Ni(AcO)_2$ PSCs.

times for precursor formation are shorter, and the times and temperatures for annealing are also lower. In particular, the energy consumption is 2.6 times higher with DMAI than with the addition of $Ni(AcO)_2$. However, the metal usage slightly increases for samples using a 0.8 M $Ni(AcO)_2$ (38.1 mol%) because of the addition of $Ni(AcO)_2$ and the higher consumption of Pb and Cs. The relative differences between the two methods are shown in the Fig. 6a.

The reduction in material and energy consumption, as well as the decrease in waste generated during spin coating, has a highly positive impact on mitigating climate change (GW), as shown in Fig. 6b, with an overall reduction of 70%. The reduction in environmental impacts is not only produced for the climate change category but for most impact categories (Fig. 6c), with an average impact reduction of 52%. The exception is the category of mineral resource use and metals (Rum) because the consumption of metals has slightly increased. The impacts considered are from cradle to gate, but if, in addition, greater stabilities and/or efficiencies are achieved with the new method, the reduction in environmental impact over the entire life cycle will be even more significant.

The impacts on human toxicity are also reduced, although to a lesser extent than in other impact categories. The synthesis of PbI_2 is primarily responsible for the impacts in these categories, as shown in Fig. 6d. In contrast, the manufacture of $Ni(AcO)_2$ accounts for only 5% of the impact in the carcinogenic human toxicity category and 2% in the non-carcinogenic human toxicity category.

In addition to the LCA, properties of concern according to harmonized classification and labeling (CLH) or notifications on classification, labeling, and packaging of substances and mixtures (CLP) (consolidated version of EC regulation no. 1272/2008) have also been considered. Lead iodide is the only substance of concern, "toxic for reproduction" (CLH), which is

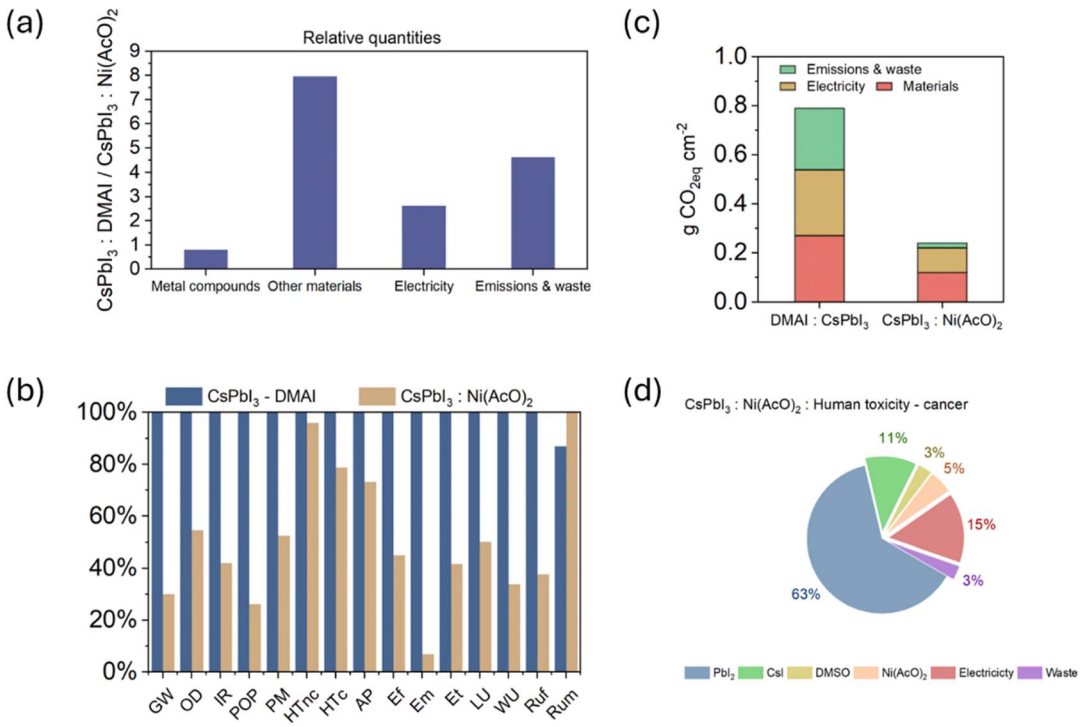

Fig. 6 (a) Relative quantities of materials, energy and wastes for 1 cm^2 of $CsPbI_3$ synthesized with DMAI in comparison with $CsPbI_3$–$Ni(AcO)_2$. (b) Comparison of absolute climate change impacts broken down into materials, electricity, emissions and waste. (c) Relative impacts for the two methods to synthesize $CsPbI_3$ (absolute values and meaning of abbreviations are listed in the Table S11). (d) Breakdown of the potential human toxicity-cancer impact for $CsPbI_3$–$Ni(AcO)_2$, whose contribution is only 5% of the total.

common to both methods. The method with DMAI also uses DMF as a solvent, "toxic for reproduction" (CLH) and included in "the candidate list of substances of very high concern" (SVHC); toluene, "suspected to be toxic for reproduction" (CLH); and TOPO, "most of the data submitters agree that this substance is a skin sensitizer" (CLP). In the $Ni(AcO)_2$ method, these three substances are not employed. Instead, a new substance with properties of concern, $Ni(AcO)_2 \cdot 4H_2O$, is added, "most data submitters agree that this substance is a skin sensitizer and a respiratory sensitizer" (CLP).

Conclusions

Our synthetic approach is designed to offer a rapid-crystallization (<10 s), DMAI/HI-free approach, and a more environmentally friendly (antisolvent and DMF-free) synthesis method to enhance the stability and performance of γ-$CsPbI_3$-$Ni(AcO)_2$ PSCs. Employing this approach, our champion device, incorporating a 7.7% mol of $Ni(AcO)_2$, exhibits a PCE exceeding 12% in a n–i–p mesoscopic configuration with a lifetime of >600 h at MPP with minimum losses (<20%). The tests performed under low-intensity illumination (cool and warm white illuminations) exhibit promising efficiencies over 15 and 17%, highlighting the potential of $CsPbI_3$–$Ni(AcO)_2$ PSCs for efficient energy harvesting in low-intensity illumination environments. Moreover, the new synthesis method with $Ni(AcO)_2$ reduces by 70% the GW and most of the impact categories. The addition of $Ni(AcO)_2$, potentially harmful for skin and respiratory sensitizing, has a low impact on human toxicity categories, which are highly affected by lead iodide. In addition, our DMSO-only method avoids the use of different substances with properties of concern, such as DMF, toluene, and TOPO. Nevertheless, these improvements should be viewed with caution, as substances of concern ($Ni(AcO)_2$ and PbI_2) persist in the absorbing layer.

We believe that our straightforward, DMSO-only, DMAI/HI-free and antisolvent-free synthetic approach paves the way for the development of highly efficient and stable all-inorganic perovskite materials for photovoltaics.

Experimental section

Chemicals

CsI (99.999%, Sigma-Aldrich), lead(II) iodide (PbI_2, 99.99%, TCI), dimethyl sulfoxide (DMSO, 99.9%, Sigma-Aldrich), isopropanol (IPA, 98%, Avantor), chlorobenzene (99.8%, Sigma-Aldrich), tris(2-(1*H*-pyrazol-1-yl)-4-*tert*-butylpyridine)cobalt(III) tri[bis-(trifluoromethane) sulfonimide] (FK209, Sigma Aldrich), 30 NR-D transparent titania paste (GreatCell Solar Materials), bis(trifluoromethane)sulfonimide lithium salt (Li-TFSI, Sigma-Aldrich), ethanol (99.9%, Merck), spiro-OMeTAD (Lumtec), titanium diisopropoxide bis(acetylacetonate) (TIAP, 75 wt% in isopropanol, Sigma-Aldrich), 4-*tert*-butyl pyridine (tBP 98%, Sigma-Aldrich), nickel(II) acetate tetrahydrate ($Ni(AcO)_2 \cdot 4H_2O$, 99% Thermo Scientific Chemicals). All chemicals are used as received.

FTO substrates cleaning

Unpatterned FTO substrates are used (TEC 15, Ossila, with dimensions 2 cm × 1.5 cm). Substrates are cleaned with 2% Extran solution with a very fine brush to clean the FTO surface, then washed with distilled water to remove soap contents. Afterwards cleaned with ethanol, acetone and isopropanol for 15 min by sonication. After drying with a nitrogen gun, the substrates are placed in a UV-ozone cleaner for 15 minutes right before the titanium oxide layer deposition.

Solution preparation

2% Extran solution is made by mixing 20 mL in 1000 mL distilled water.

TiO_2 solution is prepared by adding 1000 μL TIAP into 9 mL of ethanol.

1.5 M CsI solution is prepared by dissolving 1.063 g of CsI solution in 2.726 mL DMSO solvent. The mixture is stirred 30 minutes until complete solubilization of CsI to get the solution.

To get 1.3 M $CsPbI_3$ solution, 2.274 mL CsI solution is added in 1.145 g PbI_2 salt and stirred for 30 min at 80 °C until it completely dissolved.

To make 1.3 : 0.1 (molar ratio) $CsPbI_3$: $Ni(AcO)_2$ solution, 1 mL above CsPbI3 solution is added to 0.025 g of $Ni(AcO)_2$ and stirred for 30 min until a clear, green-yellowish perovskite solution is formed.

A 70 mM solution of spiro-OMeTAD is prepared by dissolving 90 mg spiro-OMeTAD in 982.26 μL chlorobenzene with 35.5 μL tBP, 20.40 μL LiTFSI with a stock solution of 520 mg mL^{-1} in acetonitrile, and 22.22 μL FK209 with a stock solution of 375 mg mL^{-1} in acetonitrile.

Device fabrication

TiO_2 compact layer. TiO_2 compact layer is deposited by spray pyrolysis with oxygen as the carrier gas. One edge of each substrate is covered by around 5 mm using a guided-metal holder containing the substrates of conductive FTO to avoid the side being exposed. Then the substrates are heated up to 450 °C and are kept at this temperature for 15 min before and 30 min after the spray of the precursor solution. The whole solution is transferred into a spray nozzle and sprayed at roughly 25 cm away from the substrates with an inclination angle of 45°, with at least 20 seconds of delay between each spraying cycle. Afterward, substrates are left to cool down to room temperature and then put in an ozone chamber for 15 minutes before perovskite film deposition.

TiO_2 mesoscopic layer. TiO_2 compact layer is deposited by spin coating. The as-prepared TiO_2 compact layers are coated using 70 mL of 30-NRD titania paste solution (150 mg mL^{-1} in Ethanol). The spinning time is set at 20 s at 4000 rpm. Following the deposition step the substrates are annealed all at once starting from 100 °C as sequentially deposited and then heated up to 450 °C for 30 min.

Deposition of perovskite films. Substrates are transferred into a glove box filled with nitrogen (O_2 < 0.1 ppm, H_2O < 0.1 ppm). The substrates are placed on a hot plate at 100 °C for

5 min before perovskite deposition. 50 μL perovskite solution is added and spin-coated quickly at 4000 rpm for 40 seconds. The wet films are then annealed at 75 °C for roughly 10 s and then transferred to a different hot plate at 200 °C for a 10 s fast crystallization.

Hole transport layer deposition. 50 μL spiro-OMeTAD solution is dynamic-deposited by spin coating at 4000 rpm for 30 seconds accelerating at 800 rpm s^{-1} depositing the solution after 3 s starting the program. Afterward, all the samples are transferred into a dry air box (relative humidity (RH) < 20%) for oxygen soaking.

Deposition of metal contact. Gold is evaporated using a thermal evaporator under a vacuum of approximately 10^{-6} mbar. The deposition rate is programmed at 0.02 Å s^{-1} for the first 1 nm, 0.1–0.2 Å s^{-1} for the following 5 nm, then 0.5 Å s^{-1} until 20 nm and then 1 Å s^{-1} for the rest of the deposition. Overall, it takes around 25 min for the deposition of 80 nm of gold.

Structural and optical characterization. Morphological analysis is conducted using a HITACHI S-4800 field-emission scanning electron microscope (SEM) operating at 20 kV. Crystalline structure is determined by X-ray diffraction (XRD) using a PANalytical Empyrean X-ray diffractometer with Cu Kα radiation ($\lambda = 1.5406$ Å), covering a Bragg angle range of 4–60° with a step size of 0.026°. UV-visible (UV-vis) measurements are conducted using a Shimadzu UV-2501PC spectrophotometer. All PL spectra are obtained with a CW GaN laser (404 nm). Photoluminescence (PL) characterization is conducted using an Edinburgh Instruments FLS 1000 spectrometer equipped with a double-grating Czerny–Turner monochromator for excitation and detection. The detection system, featuring a high-speed photomultiplier tube (PMT) in a cooled housing, is used to record both steady-state PL Spectra. XPS measurements are performed in a Thermo Scientific K-alpha X-ray photoelectron spectrometer system (based pressure 4×10^{-9} mbar). Photoelectrons are excited with Al Kα line 1486.6 eV of a monochromatized X-ray source. Measurements are taken at room temperature with a pass energy of 20 eV, with a spot size 400 μm.

Electrical characterization. *J–V* curve measurements are conducted under ambient conditions using an Ossila class AAA solar simulator and an automated *J–V* measurement system (T2003B3-G2009A1). The light intensity was calibrated to 1 sun (100 mW cm^{-2}) with a certified Si solar cell (RERA Solutions, RQN3290, RQN001). Measurements are performed without encapsulation at an ambient temperature of ~25 °C and RH < 10%, with an active device area of 0.026 cm^2 defined by a mask.

The MPP of the solar cells is evaluated under nitrogen (N_2) atmosphere. The stability protocol involved measuring an initial *J–V* curve to determine the maximum power point voltage (V_{max}), which is then applied to the cell for 1 hour under continuous illumination. After each hour, a new *J–V* curve is recorded to update the V_{max}, which is subsequently applied for the next hour. Solar cell parameters are monitored and recorded after each *J–V* measurement throughout the MPP. Enhanced low-intensity illuminations are obtained using the same Ossila class AAA solar simulator selecting the "cool white" and "warm white" LEDs from the software.

Conflicts of interest

The authors declare no conflict of interest.

Data availability

The data supporting the findings of this study are available from the corresponding author upon request. Supplementary information is available, see DOI: **https://doi.org/10.1039/d5el00064e**.

Acknowledgements

We acknowledge funding by the Horizon Europe project HEPAFLEX under grant agreement No. 101122345. Also, P. P. B thanks Generalitat Valenciana for the funding *via* Pla Gent-T (grant ESGENT 010/2024). M. M. A acknowledges her predoctoral contract with reference PRE2021-099951 funded by MCIN/AEI/10.13039/501100011033 as part of the project PID2020-119628RB-C31. J. N.-G. acknowledges his FPU PhD contract with reference FPU19/04544. M. V.-P. was supported by the Margarita Salas postdoctoral contract MGS/2022/16(UP2021-021) financed by the European Union-NextGenerationEU. R. V. and J-A. A-B acknowledge financial support for project PRINT-P (MFA/202/020) that forms part of the Advanced Materials programme and was supported by MCIN with funding from European Union NextGenerationEU (PRTR-C17. I1) and by Generalitat Valenciana, to the project Step-Up (CIPROM/2021/078) funded by MCIN/AEI and to the project Q-Solutions (TED2021-131600B-C31) funded by Generalitat Valenciana *via* PROMETEO. M.V.-P. was supported by the "Margarita Salas" postdoctoral contract MGS/2022/16/(UP2021-021).

References

1 A. Kojima, K. Teshima, Y. Shirai and T. Miyasaka, Organometal Halide Perovskites as Visible-Light Sensitizers for Photovoltaic Cells, *J. Am. Chem. Soc.*, 2009, **131**(17), 6050–6051, DOI: **10.1021/ja809598r**.

2 NREL, *Best Research-Cell Efficiency Chart*, **https://www.nrel.gov/pv/assets/pdfs/best-research-cell-efficiencies.pdf** accessed 2024-07-18.

3 G. M. Meheretu, A. K. Worku, M. T. Yihunie, R. K. Koech and G. A. Wubetu, The Recent Advancement of Outdoor Performance of Perovskite Photovoltaic Cells Technology, *Heliyon*, 2024, **10**(17), e36710, DOI: **10.1016/j.heliyon.2024.e36710**.

4 J. Zhao, Y. Deng, H. Wei, X. Zheng, Z. Yu, Y. Shao, J. E. Shield and J. Huang, Strained Hybrid Perovskite Thin Films and Their Impact on the Intrinsic Stability of Perovskite Solar Cells, *Sci. Adv.*, 2017, **3**(11), eaao5616, DOI: **10.1126/sciadv.aao5616**.

5 S. Khatoon, S. Kumar Yadav, V. Chakravorty, J. Singh, R. Bahadur Singh, M. S. Hasnain and S. M. M. Hasnain,

Perovskite Solar Cell's Efficiency, Stability and Scalability: A Review, *Mater. Sci. Energy Technol.*, 2023, **6**, 437–459, DOI: 10.1016/j.mset.2023.04.007.

6 N. Ahn and M. Choi, Towards Long-Term Stable Perovskite Solar Cells: Degradation Mechanisms and Stabilization Techniques, *Advanced Science*, 2024, **11**(4), 2306110, DOI: 10.1002/advs.202306110.

7 D. Zhang, D. Li, Y. Hu, A. Mei and H. Han, Degradation Pathways in Perovskite Solar Cells and How to Meet International Standards, *Commun. Mater.*, 2022, **3**(1), 1–14, DOI: 10.1038/s43246-022-00281-z.

8 R. J. Sutton, M. R. Filip, A. A. Haghighirad, N. Sakai, B. Wenger, F. Giustino and H. J. Snaith, Cubic or Orthorhombic? Revealing the Crystal Structure of Metastable Black-Phase CsPbI3 by Theory and Experiment, *ACS Energy Lett.*, 2018, **3**(8), 1787–1794, DOI: 10.1021/acsenergylett.8b00672.

9 A. Marronnier, G. Roma, S. Boyer-Richard, L. Pedesseau, J.-M. Jancu, Y. Bonnassieux, C. Katan, C. C. Stoumpos, M. G. Kanatzidis and J. Even, Anharmonicity and Disorder in the Black Phases of Cesium Lead Iodide Used for Stable Inorganic Perovskite Solar Cells, *ACS Nano*, 2018, **12**(4), 3477–3486, DOI: 10.1021/acsnano.8b00267.

10 Y. Jiang, J. Yuan, Y. Ni, J. Yang, Y. Wang, T. Jiu, M. Yuan and J. Chen, Reduced-Dimensional α-CsPbX3 Perovskites for Efficient and Stable Photovoltaics, *Joule*, 2018, **2**(7), 1356–1368, DOI: 10.1016/j.joule.2018.05.004.

11 A. Swarnkar, A. R. Marshall, E. M. Sanehira, B. D. Chernomordik, D. T. Moore, J. A. Christians, T. Chakrabarti and J. M. Luther, Quantum Dot–Induced Phase Stabilization of α-CsPbI3 Perovskite for High-Efficiency Photovoltaics, *Science*, 2016, **354**(6308), 92–95, DOI: 10.1126/science.aag2700.

12 S. Hu, A. R. Tapa, X. Zhou, S. Pang, M. Lira-Cantu and H. Xie, Formation and Stabilization of Metastable Halide Perovskite Phases for Photovoltaics, *Cell Rep. Phys. Sci.*, 2024, **5**(2), 101825, DOI: 10.1016/j.xcrp.2024.101825.

13 S.-F.-A. Shah, I. Jeong, J. Park, D. Shin, I. Hwang, N. Tsvetkov, D. Kim, J. Gwak, J. H. Park, S. I. Seok, K. Kim and H. Min, Efficient and Stable CsPbI3 Perovskite Solar Cells with Spontaneously Formed 2D-$Cs_2PbI_2Cl_2$ at the Buried Interface, *Cell Rep. Phys. Sci.*, 2024, **5**(5), 101935, DOI: 10.1016/j.xcrp.2024.101935.

14 A. Al-Ashouri, E. Köhnen, B. Li, A. Magomedov, H. Hempel, P. Caprioglio, J. A. Márquez, A. B. Morales Vilches, E. Kasparavicius, J. A. Smith, N. Phung, D. Menzel, M. Grischek, L. Kegelmann, D. Skroblin, C. Gollwitzer, T. Malinauskas, M. Jošt, G. Matič, B. Rech, R. Schlatmann, M. Topič, L. Korte, A. Abate, B. Stannowski, D. Neher, M. Stolterfoht, T. Unold, V. Getautis and S. Albrecht, Monolithic Perovskite/Silicon Tandem Solar Cell with >29% Efficiency by Enhanced Hole Extraction, *Science*, 2020, **370**(6522), 1300–1309, DOI: 10.1126/science.abd4016.

15 H. Li and W. Zhang, Perovskite Tandem Solar Cells: From Fundamentals to Commercial Deployment, *Chem. Rev.*, 2020, **120**(18), 9835–9950, DOI: 10.1021/acs.chemrev.9b00780.

16 W. Shockley and H. J. Queisser, Detailed Balance Limit of Efficiency of P–n Junction Solar Cells, *J. Appl. Phys.*, 1961, **32**(3), 510–519, DOI: 10.1063/1.1736034.

17 J. K. W. Ho, H. Yin and S. K. So, From 33% to 57% – an Elevated Potential of Efficiency Limit for Indoor Photovoltaics, *J. Mater. Chem. A*, 2020, **8**(4), 1717–1723, DOI: 10.1039/C9TA11894B.

18 D. Xu, M. Wu, Y. Bai, B. Wang, H. Zhou, Z. Fan, N. Zhang, J. Tan, H. Li, H. Bian and Z. Liu, Record-Efficiency Inverted $CsPbI_3$ Perovskite Solar Cells Enabled by Rearrangement and Hydrophilic Modification of SAMs, *Adv. Funct. Mater.*, 2025, **35**(2), 2412946, DOI: 10.1002/adfm.202412946.

19 J. Qiu, X. Mei, M. Zhang, G. Wang, S. Zou, L. Wen, J. Huang, Y. Hua and X. Zhang, Dipolar Chemical Bridge Induced $CsPbI_3$ Perovskite Solar Cells with 21.86% Efficiency, *Angew. Chem., Int. Ed.*, 2024, **63**(18), e202401751, DOI: 10.1002/anie.202401751.

20 X. Tan, S. Wang, Q. Zhang, H. Liu, W. Li, L. Zhu and H. Chen, Stabilizing $CsPbI_3$ Perovskite for Photovoltaic Applications, *Matter*, 2023, **6**(3), 691–727, DOI: 10.1016/j.matt.2022.12.012.

21 M. Wright, B. V. Stefani, T. W. Jones, B. Hallam, A. Soeriyadi, L. Wang, P. Altermatt, H. J. Snaith, G. J. Wilson and R. S. Bonilla, Design Considerations for the Bottom Cell in Perovskite/Silicon Tandems: A Terawatt Scalability Perspective, *Energy Environ. Sci.*, 2023, **16**(10), 4164–4190, DOI: 10.1039/D3EE00952A.

22 R. Montecucco, G. Pica, V. Romano, F. De Boni, S. Cavalli, G. Bruni, E. Quadrivi, M. De Bastiani, M. Prato, R. Po and G. Grancini, The Stabilization of $CsPbI_3$–Br Phase by Lowering Annealing Temperature for Efficient All-Inorganic Perovskite Solar Cells, *Sol. RRL*, 2023, **7**(20), 2300358, DOI: 10.1002/solr.202300358.

23 F. Haque, M. Wright, M. A. Mahmud, H. Yi, D. Wang, L. Duan, C. Xu, M. B. Upama and A. Uddin, Effects of Hydroiodic Acid Concentration on the Properties of CsPbI3 Perovskite Solar Cells, *ACS Omega*, 2018, **3**(9), 11937–11944, DOI: 10.1021/acsomega.8b01589.

24 Y. Gao, W. Xu, F. He, T. Fan, W. Cai, X. Zhang and G. Wei, Boosting Performance of $CsPbI_3$ Perovskite Solar Cells *via* the Synergy of Hydroiodic Acid and Deionized Water, *Adv. Energy Sustainability Res.*, 2022, **3**(2), 2100149, DOI: 10.1002/aesr.202100149.

25 B. Li, Y. Zhang, L. Fu, T. Yu, S. Zhou, L. Zhang and L. Yin, Surface Passivation Engineering Strategy to Fully-Inorganic Cubic $CsPbI_3$ Perovskites for High-Performance Solar Cells, *Nat. Commun.*, 2018, **9**(1), 1076, DOI: 10.1038/s41467-018-03169-0.

26 A. Chakrabarti, B. M. Lefler and A. T. Fafarman, Scaffold-Enforced Nanoscale Crystalline Order Supersedes Interfacial Interactions in Driving $CsPbI_3$ Perovskite Phase Stability, *J. Phys. Chem. C*, 2022, **126**(51), 21708–21715, DOI: 10.1021/acs.jpcc.2c05794.

27 A. Shpatz Dayan, B.-E. Cohen, S. Aharon, C. Tenailleau, M. Wierzbowska and L. Etgar, Enhancing Stability and Photostability of $CsPbI_3$ by Reducing Its Dimensionality,

Chem. Mater., 2018, **30**(21), 8017–8024, DOI: 10.1021/acs.chemmater.8b03709.

28 F. Li, Y. Pei, F. Xiao, T. Zeng, Z. Yang, J. Xu, J. Sun, B. Peng and M. Liu, Tailored Dimensionality to Regulate the Phase Stability of Inorganic Cesium Lead Iodide Perovskites, *Nanoscale*, 2018, **10**(14), 6318–6322, DOI: 10.1039/C8NR00758F.

29 Y. Zhang, Y. Yang, X. Zhang, T. Wang, L. Nian, Q. Rong, G. Zhou and N. Li, Low Temperature Preparation of All-Inorganic $CsPbI_3$ Perovskite Solar Cells with Ethanediamine as Additive, *Org. Electron.*, 2020, **87**, 105940, DOI: 10.1016/j.orgel.2020.105940.

30 T. Li, Y. Wu, Z. Liu, Y. Yang, H. Luo, L. Li, P. Chen, X. Gao and H. Tan, Cesium Acetate-Assisted Crystallization for High-Performance Inverted $CsPbI_3$ Perovskite Solar Cells, *Nanotechnology*, 2022, **33**(37), 375205, DOI: 10.1088/1361-6528/ac76d5.

31 X. Chang, J. Fang, Y. Fan, T. Luo, H. Su, Y. Zhang, J. Lu, L. Tsetseris, T. D. Anthopoulos, S. Liu(Frank) and K. Zhao, Printable $CsPbI_3$ Perovskite Solar Cells with PCE of 19% *via* an Additive Strategy, *Adv. Mater.*, 2020, **32**(40), 2001243, DOI: 10.1002/adma.202001243.

32 L. Duan, H. Zhang, M. Liu, M. Grätzel and J. Luo, Phase-Pure γ-$CsPbI_3$ for Efficient Inorganic Perovskite Solar Cells, *ACS Energy Lett.*, 2022, **7**(9), 2911–2918, DOI: 10.1021/acsenergylett.2c01219.

33 Y. Wang, X. Liu, T. Zhang, X. Wang, M. Kan, J. Shi and Y. Zhao, The Role of Dimethylammonium Iodide in $CsPbI_3$ Perovskite Fabrication: Additive or Dopant?, *Angew. Chem., Int. Ed.*, 2019, **58**(46), 16691–16696, DOI: 10.1002/anie.201910800.

34 M. Shekarnoush, F. S. Aguirre-Tostado and M. Q. López, Stability of $CsPbI_3$ with Divalent Cations Incorporated *via* Mechanochemical Alloying, *Mater. Adv.*, 2024, **5**(9), 3742–3750, DOI: 10.1039/D4MA00034J.

35 A. Alberti, E. Smecca, I. Deretzis, G. Mannino, C. Bongiorno, S. Valastro, S. Sanzaro, G. Fisicaro, A. K. Jena, Y. Numata, Z. Guo, C. Spinella, T. Miyasaka and A. La Magna, Formation of $CsPbI_3$ γ-Phase at 80 °C by Europium-Assisted Snowplow Effect, *Adv. Energy Sustainability Res.*, 2021, **2**(7), 2100091, DOI: 10.1002/aesr.202100091.

36 Z. Li, J. Xu, S. Zhou, B. Zhang, X. Liu, S. Dai and J. Yao, CsBr-Induced Stable CsPbI3–*x*Brx (x < 1) Perovskite Films at Low Temperature for Highly Efficient Planar Heterojunction Solar Cells, *ACS Appl. Mater. Interfaces*, 2018, **10**(44), 38183–38192, DOI: 10.1021/acsami.8b11474.

37 G. E. Eperon, G. M. Paternò, R. J. Sutton, A. Zampetti, A. A. Haghighirad, F. Cacialli and H. J. Snaith, Inorganic Caesium Lead Iodide Perovskite Solar Cells, *J. Mater. Chem. A*, 2015, **3**(39), 19688–19695, DOI: 10.1039/C5TA06398A.

38 W. Ke, I. Spanopoulos, C. C. Stoumpos and M. G. Kanatzidis, Myths and Reality of $HPbI_3$ in Halide Perovskite Solar Cells, *Nat. Commun.*, 2018, **9**(1), 1–9, DOI: 10.1038/s41467-018-07204-y.

39 H. Meng, Z. Shao, L. Wang, Z. Li, R. Liu, Y. Fan, G. Cui and S. Pang, Chemical Composition and Phase Evolution in DMAI-Derived Inorganic Perovskite Solar Cells, *ACS Energy Lett.*, 2020, **5**(1), 263–270, DOI: 10.1021/acsenergylett.9b02272.

40 Y. Jiang, T.-F. Xu, H.-Q. Du, M. U. Rothmann, Z.-W. Yin, Y. Yuan, W.-C. Xiang, Z.-Y. Hu, G.-J. Liang, S.-Z. Liu, M. K. Nazeeruddin, Y.-B. Cheng and W. Li, Organic-Inorganic Hybrid Nature Enables Efficient and Stable $CsPbI_3$-Based Perovskite Solar Cells, *Joule*, 2023, **7**(12), 2905–2922, DOI: 10.1016/j.joule.2023.10.019.

41 N. Sun, S. Fu, Y. Li, L. Chen, J. Chung, M. M. Saeed, K. Dolia, A. Rahimi, C. Li, Z. Song and Y. Yan, Tailoring Crystallization Dynamics of $CsPbI_3$ for Scalable Production of Efficient Inorganic Perovskite Solar Cells, *Adv. Funct. Mater.*, 2024, **34**(6), 2309894, DOI: 10.1002/adfm.202309894.

42 H. Bian, H. Wang, Z. Li, F. Zhou, Y. Xu, H. Zhang, Q. Wang, L. Ding, S. Liu(Frank) and Z. Jin, Unveiling the Effects of Hydrolysis-Derived DMAI/DMAPbI Intermediate Compound on the Performance of CsPbI3 Solar Cells, *Adv. Sci.*, 2020, **7**(9), 1902868, DOI: 10.1002/advs.201902868.

43 A. R. Marshall, H. C. Sansom, M. M. McCarthy, J. H. Warby, O. J. Ashton, B. Wenger and H. J. Snaith, Dimethylammonium: An A-Site Cation for Modifying CsPbI3, *Sol. RRL*, 2021, **5**(1), 2000599, DOI: 10.1002/solr.202000599.

44 J. Noguera-Gómez, I. Fernández-Guillen, P. F. Betancur, V. S. Chirvony, P. P. Boix and R. Abargues, Low-Demanding *in Situ* Crystallization Method for Tunable and Stable Perovskite Nanoparticle Thin Films, *Matter*, 2022, **5**(10), 3541–3552, DOI: 10.1016/J.MATT.2022.07.017.

45 M. Minguez-Avellan, N. Farinós-Navajas, J. Noguera-Gómez, V. Sagra Rodríguez, M. Vallés-Pelarda, C. Momblona, T. S. Ripolles, P. P. Boix and R. Abargues, Perovskite Nanocomposite: A Step Toward Photocatalytic Degradation of Organic Dyes, *Sol. RRL*, 2024, **8**(19), 2400449, DOI: 10.1002/solr.202400449.

46 J. Noguera-Gómez, P. P. Boix and R. Abargues, Protocol for the Synthesis of Perovskite Nanocrystal Thin Films *via in Situ* Crystallization Method, *STAR Protoc.*, 2023, **4**(4), 102507, DOI: 10.1016/j.xpro.2023.102507.

47 J. Noguera-Gómez, V. Sagra-Rodríguez, V. S. Chirvony, M. Minguez-Avellan, M. Eledath-Changarath, J. F. Sánchez-Royo, J. P. Martínez-Pastor, P. P. Boix and R. Abargues, Passivation Mechanism in Highly Luminescent Nanocomposite-Based $CH_3NH_3PbBr_3$ Perovskite Nanocrystals, *Small Sci.*, 2025, **5**(5), 2400529, DOI: 10.1002/smsc.202400529.

48 S. Soriano-Díaz, J. Noguera-Gómez, J. P. Martínez-Pastor, P. P. Boix, R. Abargues and I. Suárez, Photon Recycling Triggered Amplified Spontaneous Emission in $MAPbBr_3$-$Ni(AcO)_2$ Nanocomposite Waveguides, *Laser Photonics Rev.*, 2025, **19**(10), 2401920, DOI: 10.1002/lpor.202401920.

49 R. J. Elliott, Intensity of Optical Absorption by Excitons, *Phys. Rev.*, 1957, **108**(6), 1384–1389, DOI: 10.1103/PhysRev.108.1384.

50 J. T.-W. Wang, Z. Wang, S. Pathak, W. Zhang, D. W. deQuilettes, F. Wisnivesky-Rocca-Rivarola, J. Huang, P. K. Nayak, J. B. Patel, H. A. Mohd Yusof, Y. Vaynzof,

R. Zhu, I. Ramirez, J. Zhang, C. Ducati, C. Grovenor, M. B. Johnston, D. S. Ginger, R. J. Nicholas and H. J. Snaith, Efficient Perovskite Solar Cells by Metal Ion Doping, *Energy Environ. Sci.*, 2016, **9**(9), 2892–2901, DOI: **10.1039/C6EE01969B**.

51 L. McGovern, I. Koschany, G. Grimaldi, L. A. Muscarella and B. Ehrler, Grain Size Influences Activation Energy and Migration Pathways in $MAPbBr_3$ Perovskite Solar Cells, *J. Phys. Chem. Lett.*, 2021, **12**(9), 2423–2428, DOI: **10.1021/acs.jpclett.1c00205**.

52 H. Zhao, Z. Xu, Y. Che, Y. Han, S. Yang, C. Duan, J. Cui, S. Dai, Z. Liu and S. Liu(Frank), Simultaneous Dual-Interface and Bulk Defect Passivation for High-Efficiency and Stable $CsPbI_2Br$ Perovskite Solar Cells, *J. Power Sources*, 2021, **492**, 229580, DOI: **10.1016/j.jpowsour.2021.229580**.

53 W. Tress, M. Yavari, K. Domanski, P. Yadav, B. Niesen, J. P. C. Baena, A. Hagfeldt and M. Graetzel, Interpretation and Evolution of Open-Circuit Voltage, Recombination, Ideality Factor and Subgap Defect States during Reversible Light-Soaking and Irreversible Degradation of Perovskite Solar Cells, *Energy Environ. Sci.*, 2018, **11**(1), 151–165, DOI: **10.1039/C7EE02415K**.

54 K.-L. Wang, H. Lu, M. Li, C.-H. Chen, D. Bo Zhang, J. Chen, J.-J. Wu, Y.-H. Zhou, X.-Q. Wang, Z.-H. Su, Y.-R. Shi, Q.-S. Tian, Y.-X. Ni, X.-Y. Gao, S. M. Zakeeruddin, M. Grätzel, Z.-K. Wang and L.-S. Liao, Ion–Dipole Interaction Enabling Highly Efficient CsPbI3 Perovskite Indoor Photovoltaics, *Adv. Mater.*, 2023, **35**(31), 2210106, DOI: **10.1002/adma.202210106**.

55 C. F. J. Lau, Z. Wang, N. Sakai, J. Zheng, C. H. Liao, M. Green, S. Huang, H. J. Snaith and A. Ho-Baillie, Fabrication of Efficient and Stable $CsPbI_3$ Perovskite Solar Cells through Cation Exchange Process, *Adv. Energy Mater.*, 2019, **9**(36), 1901685, DOI: **10.1002/aenm.201901685**.

56 R. Frischknecht, *Methodology Guidelines on Life Cycle Assessment of Photovoltaic*, 2020.

57 Z. Iqbal, F. Zu, A. Musiienko, E. Gutierrez-Partida, H. Köbler, T. W. Gries, G. V. Sannino, L. Canil, N. Koch, M. Stolterfoht, D. Neher, M. Pavone, A. B. Muñoz-García, A. Abate and Q. Wang, Interface Modification for Energy Level Alignment and Charge Extraction in $CsPbI_3$ Perovskite Solar Cells, *ACS Energy Lett.*, 2023, **8**(10), 4304–4314, DOI: **10.1021/acsenergylett.3c01522**.

58 Joint Research (European Commission), R. Pant and L. Zampori, *Suggestions for Updating the Organisation Environmental Footprint (OEF) Method*, Publications Office of the European Union, 2019.